

*Grant/ Marshall*

*38p.*

FINAL TECHNICAL REPORT:  
FURTHER STUDIES WITH DATA COLLECTED BY NASA'S  
AIRBORNE DOPPLER LIDAR IN OKLAHOMA IN 1981

Sept. 1985 - Aug. 1986

*IN-47*

Purchase Order No. H-78746B

*29614*

by

Howard B. Bluestein and Eugene W. McCaul, Jr.,  
Cooperative Institute for Mesoscale Meteorological Studies  
and  
University of Oklahoma, School of Meteorology,  
Norman, Oklahoma 73019

October 1986

Prepared for George C. Marshall Space Flight Center,  
Marshall Space Flight Center, Alabama 35812

(NASA-CR-179779) FURTHER STUDIES WITH DATA N87-10660  
COLLECTED BY NASA'S AIRBORNE DOPPLER LIDAR  
IN OKLAHOMA IN 1981 Final Technical Report,  
Sep. 1985 - Aug. 1986 (Oklahoma Univ.) 38 p Unclas  
CSCL 04B G3/47 44280

## PREFACE

This is a report of work which is an extension of that reported in NASA Contractor Report 3960 entitled "Analysis of Airborne Doppler Lidar, Doppler Radar, and Tall Tower Measurements of Atmospheric Flows in Quiescent and Stormy Weather." The focus here is on more Doppler lidar observations in thunderstorm environments. This study has led to two publications in refereed journals: One appeared in Applied Optics, and the other will appear in the Journal of Atmospheric and Oceanic Technology.

## TABLE OF CONTENTS

Preface.....	ii
1. Introduction.....	1
2. Refinements to Data Analysis.....	3
2.1. Consistency checks: general procedures.....	4
2.2. Consistency checks of intensity data.....	6
2.3. Consistency checks of spectral width data.....	6
3. Other Analyses.....	15
3.1. Vorticity analysis along the run 2 gust front....	15
3.2. Divergence near an isolated cumulus congestus....	26
4. Summary.....	31
5. References.....	33
Appendix A:	
Abstracts of Papers Resulting From This Project.....	35
A.1. Observations of Oklahoma severe thunderstorms using airborne Doppler lidar data.....	36
A.2. Airborne Doppler lidar techniques for observing severe thunderstorms.....	41
A.3. Airborne Doppler lidar observations of convective phenomena in Oklahoma.....	42

## Chapter I

### INTRODUCTION

Bluestein et al. (1985) describe a number of interesting findings in their analyses of data obtained in Oklahoma in 1981 using the Airborne Doppler Lidar System (ADLS) developed by the National Aeronautics and Space Administration's (NASA) Marshall Space Flight Center. Vortices were observed along thunderstorm gust fronts, and patterns of convergence were noted along the sides of an isolated cumulus congestus, suggesting that the instrument could prove useful in studies of various "clear air" convective phenomena not currently observable in any detail with Doppler radars. However, the complexity of the data, along with the presence of several systematic errors associated with delays in data recording, made it imperative that careful attention to data quality control be exercised in the interpretation of results derived from the data.

A number of substantial refinements to the previous data analysis algorithms have been made during the course of work supported by this contract, in an attempt to improve the internal consistency of the data and enhance the reliability of the analyses. In making these refinements we have attempted to exploit more fully some of the built-in

redundancy of the measurements of scalar quantities which attends the use of intersecting lines of sight needed in the synthesis of the coplane wind fields. The more substantial of these refinements are discussed below. Results of analyses based on use of the refined algorithms shows that the scalar intensity field estimates are quite stable and reliable, while the scalar spectral width field estimates, after removal of the effects of mean radial velocity gradients, are reliable as long as the intensity of the echo is sufficiently strong.

## Chapter II

### REFINEMENTS TO DATA ANALYSES

During intercomparison tests made between the 1981 lidar data and data from radars and other sensors, it became clear that certain of the lidar data fields could not easily be compared directly to any quantities obtained from other instruments. The lidar echo intensities are an obvious example, but the lidar spectral widths were also difficult to compare with those from a Doppler radar due to the high noise content of the latter's estimates in clear air near storm edges. In the absence of credible reference data with which to compare the lidar intensities and widths, it became necessary to seek a more self-contained method of evaluating the reliability of those estimates. The fore and aft measurements of wind components are necessary in the deduction of the two-dimensional wind vectors, but companion fore/aft measurements of scalar fields are once-redundant and thus offer a built-in opportunity for internal consistency checks in the lidar data. In this section we describe the development of the algorithms used in applying these consistency checks to the intensity and spectral width data from the 1981 experiments.

### 2.1. Consistency checks: general procedures

The first step in the internal consistency checks for the scalar lidar data fields is segregation of fore and aft scan data and application of thresholding and point-editing routines (Bluestein et al., 1985; McCaul, 1985) to remove obviously noisy data which would not benefit from the correction procedures to be described below. Initially, thresholding parameters were set to values used in earlier analyses. Later, however, after examining the data using the consistency algorithms, we found that revised thresholding values could be used and conditional relationships specified between those values, so that the thresholding algorithm would perform more efficiently during final data analyses. As an additional precaution, range averages of the intensity and spectral width data were computed; in some cases, frame biases similar to those seen in the velocities (see Bluestein et al., 1985) were observed. The source of these frame biases in intensity and width is not known, but may originate in small fluctuations of transmitted laser power. In any case, the biases were reduced by application of the bias removal technique described in Bluestein et al. (1985). After thresholding, editing, and frame-bias removal, independent objective analyses of fore and aft scalar fields were performed and the results plotted for comparison purposes. Areas of significant disagreement could then be identified and their

relationship to raw signal-to-noise ratio (SNR) could be studied. Following removal of data in the areas subject to significant disagreement, final analyses of the data could be prepared by averaging the fore and aft fields of gridded data at those grid points where both fields were in agreement.

Due to the time lags between fore and aft data collected at longer ranges from the aircraft, agreement between fore and aft fields was not always perfect, even when data advection (Bluestein et al., 1985; McCaul, 1985) was used prior to the interpolation of raw data to the Cartesian grid. Some flexibility was found to be needed in choosing the criteria for agreement between fore and aft fields, because of the possibility of large local differences between fields in areas of large gradients. Choices of agreement criteria which imposed too stringent a requirement for agreement were found to result in undesirable deletion of valid data in these gradient regions. Ideally the comparison of fore and aft fields should consist of two-dimensional cross-covariance calculations and additional correction for any field displacements inferred from them, followed by comparison of the fields using more stringent comparison criteria than were used here. However, this procedure would have been too cumbersome for normal use. Instead, it was more practical to employ loose comparison criteria in conjunction with detailed subjective review of

plotted results and some point editing in order to achieve the optimum analyses of the data.

### 2.2. Consistency checks of intensity data

In comparing the fore and aft fields of relative reflectivity, it was found that agreement between the independent fields was excellent. Examples of the fore and aft fields from run 2 are shown in Figs. 1 and 2. Because of the presence of large gradients of reflectivity along the arcus cloud in run 2, it was necessary to establish a rather loose comparison criterion for determining whether the fields were in agreement. The criterion for agreement was that the ratio of fore and aft relative reflectivities at grid points be within 20 dB of each other. The similarity of the fields in Figs. 1-2 is evidence that the relative reflectivity field is internally consistent, and almost certainly measures some physically meaningful atmospheric quantity related to water vapor or cloud density.

### 2.3. Consistency checks of spectral width data

Comparison of the fore and aft fields of raw spectral width data interpolated to grid points showed that there were substantial areas of disagreement between the fields. The areas of disagreement were apparent near the velocity gradient of the gust front; disagreement was also noted along the entire run at long ranges from the aircraft.

ORIGINAL PAGE IS  
OF POOR QUALITY

FIG. 1. Relative reflectivity from fore data, run 2, 30 June 1981.

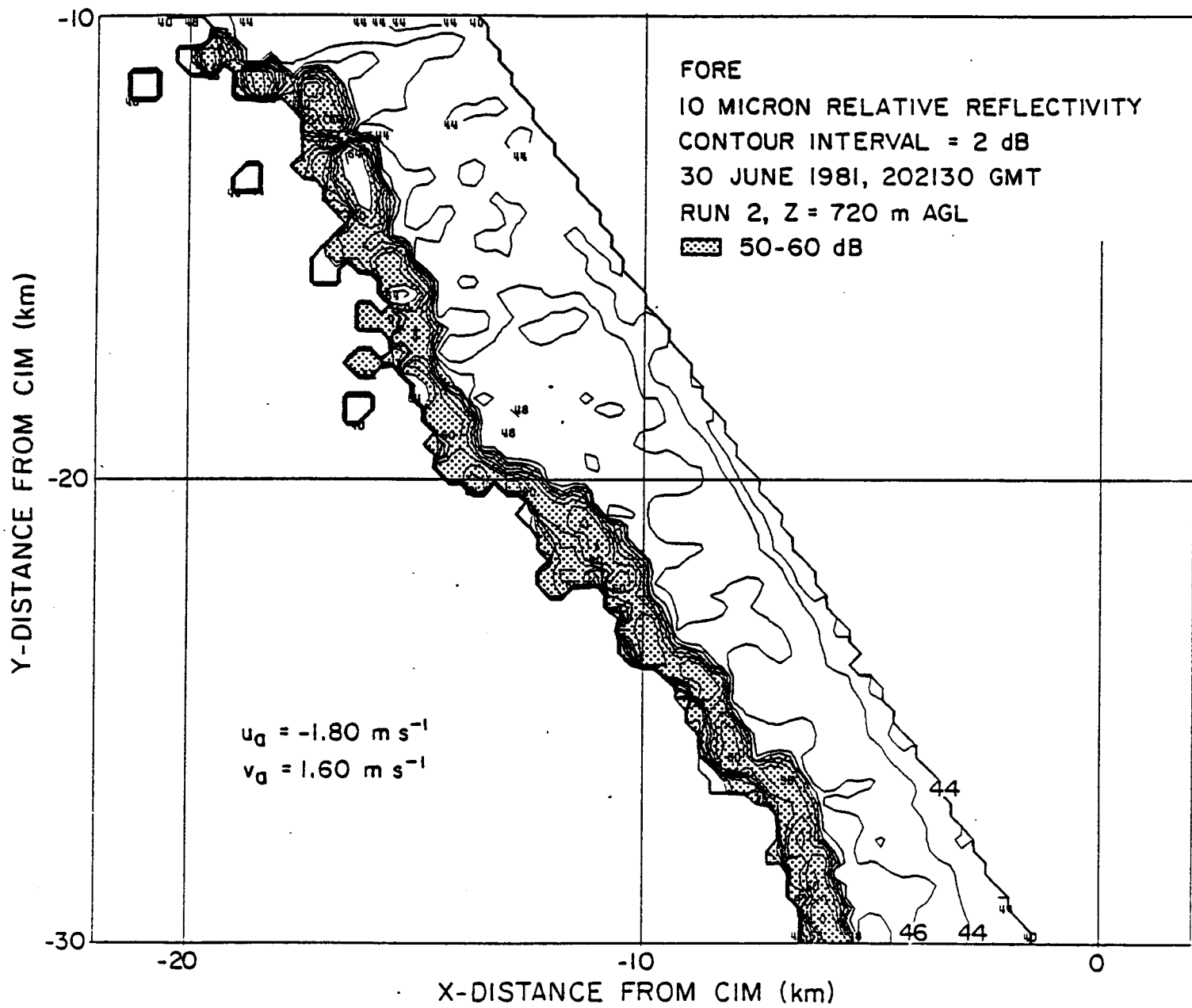
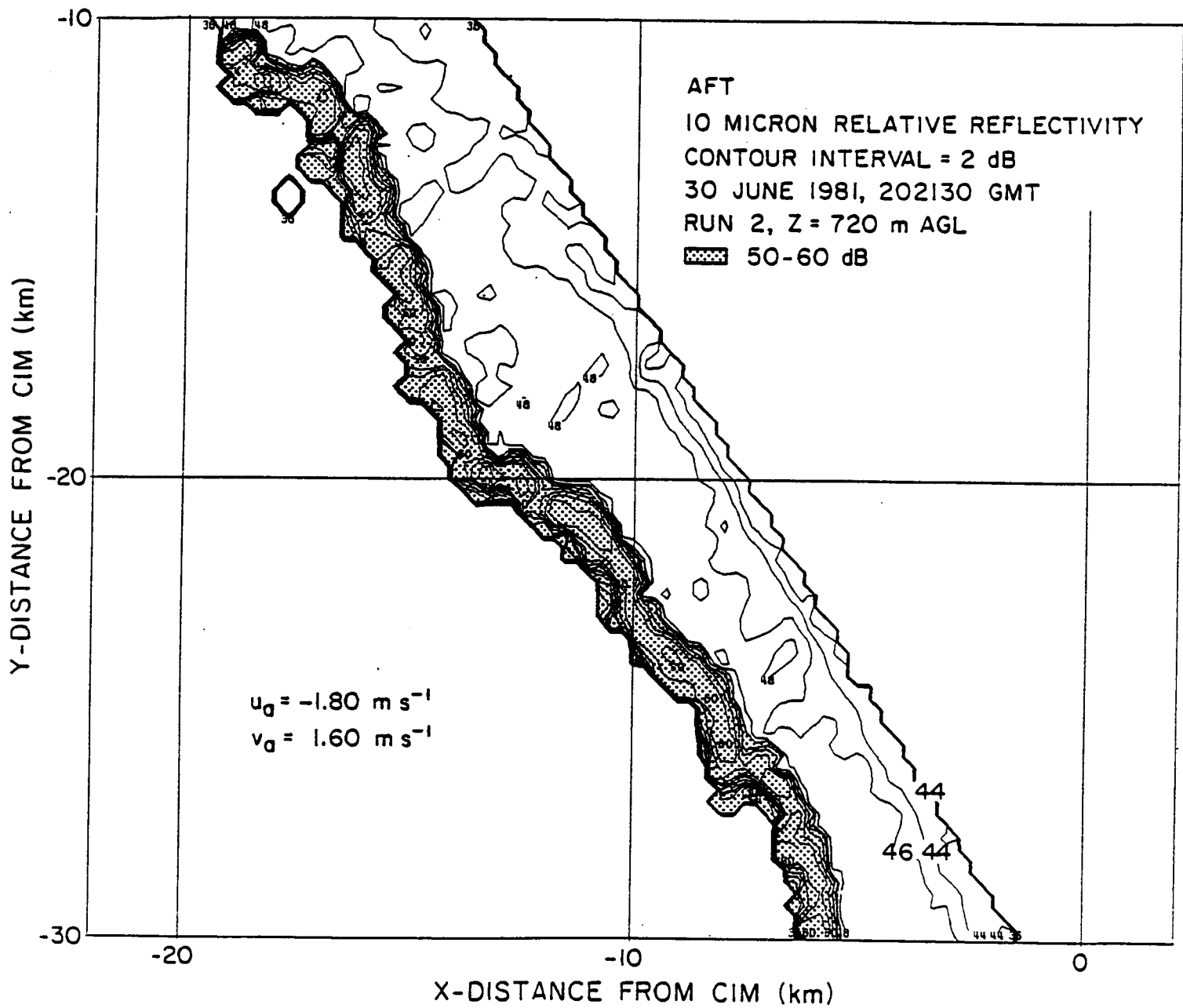


FIG. 2. Relative reflectivity from aft data, run 2, 30 June 1981.



Study of this disagreement between fore and aft spectral width fields eventually revealed that there were two factors responsible for the disagreement.

The first factor relates to the unavoidable increase of noise in the spectral width estimates as the raw SNR is reduced. Since SNR normally declines with range - unless highly reflective targets are encountered - we expect the spectral widths to become noisy beyond a certain range corresponding to a critical value of SNR. Through study of the differences between fore and aft spectral widths it was observed that noise overwhelmed the spectral width estimates whenever the SNR was not at least 12 dB. This background noise level is easily estimated by examining the raw SNR at long ranges from the aircraft. The noisy portion of the spectral width fields associated with low SNR were thus removed from the data by thresholding out those width values which were unreasonably large and which were collected in regions where SNR was less than 12 dB.

The second factor which caused disagreement between fore and aft spectral widths, sometimes even at high SNR, was ultimately discovered to be the presence of radial velocity gradients along lidar lines of sight. Since the mean velocity field was highly anisotropic, fore and aft lines of sight generally did not see the same gradients of velocity because of their different angles of incidence. These

different mean velocity gradients were capable of introducing significantly different components of apparent spectral width in fore and aft spectral width estimates. In order to remove these anisotropic effects from the spectral width estimates and obtain revised estimates which would more accurately reflect the more isotropic effects of turbulent velocity fluctuations, we attempted to remove that portion of each spectral width estimate due to the gradient of radial velocity. The simple model we developed to assess the effect of radial velocity gradients on spectral width is described below.

We first assume that we may describe the radial velocity  $v_r$  as a locally linear function of range about some range  $r_0$ :

$$v_r = v_r(r_0) + (r - r_0) \partial v_r / \partial r \quad (1)$$

Under this assumption the probability density function  $P(v_r)$  is uniform across the velocity interval defined from the difference of radial velocities at the range gates "j+1" and "j-1" adjacent to any range gate "j" at  $r=r_0$ , where we wish to correct the spectral width. We thus compute  $P(v_r)$  from:

$$P(v_r) = \frac{1}{\Delta r \cdot \partial v_r / \partial r} \quad (2)$$

In equation (2) we specify  $\Delta r$  as the range gate depth and estimate the derivative  $\partial V_r / \partial r$  by centered finite differences. Now we may obtain an expression for the spectral width due to the mean velocity gradient from:

$$\sigma_v^2 = \int_{V_1}^{V_2} V_r^2 P(V_r) dV_r \quad (3)$$

where the limits  $V_1$  and  $V_2$  are given respectively by  $-(\partial V_r / \partial r)(\Delta r / 2)$  and  $+(\partial V_r / \partial r)(\Delta r / 2)$ . Integration of (3) produces:

$$\sigma_v^2 = (\partial V_r / \partial r)^2 (\Delta r)^2 / 12 \quad (4)$$

We now simply assume that the total measured spectral width squared consists of the sum of the squared widths  $\sigma_v^2$  due to mean velocity gradients and  $\sigma_t^2$  due to turbulent fluctuations within the range resolution volume. We thus write:

$$\sigma^2 = \sigma_v^2 + \sigma_t^2 \quad (5)$$

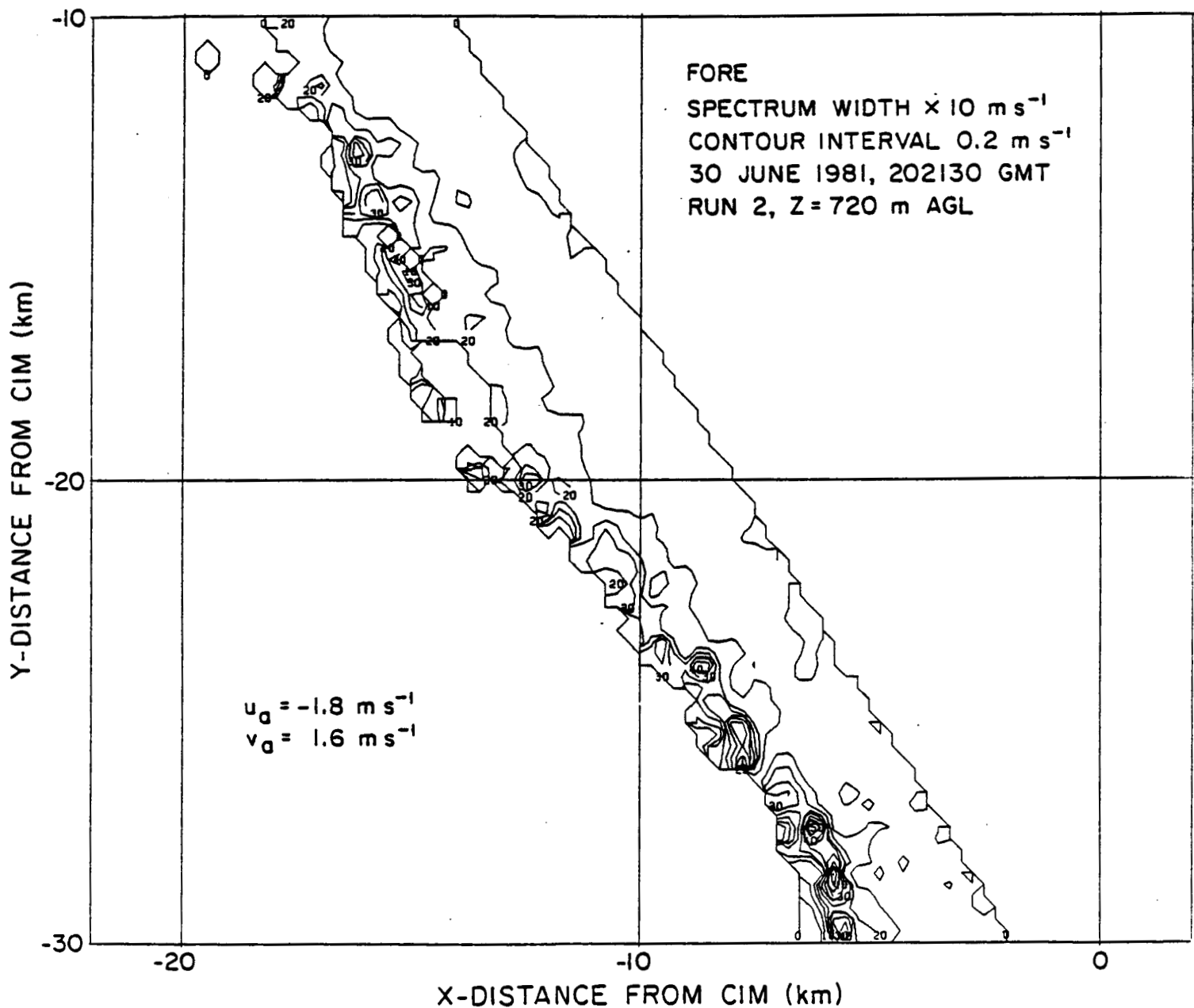
To obtain the estimate of turbulent spectral width we transpose (5) to get:

$$\sigma_t = (\sigma^2 - \sigma_v^2)^{1/2} \quad (6)$$

subject to the constraint that if the radicand in (6) is negative then the turbulent width estimate is zero. Tests of this formula on even large data runs yielded only a handful of points where the radicand in (6) was negative.

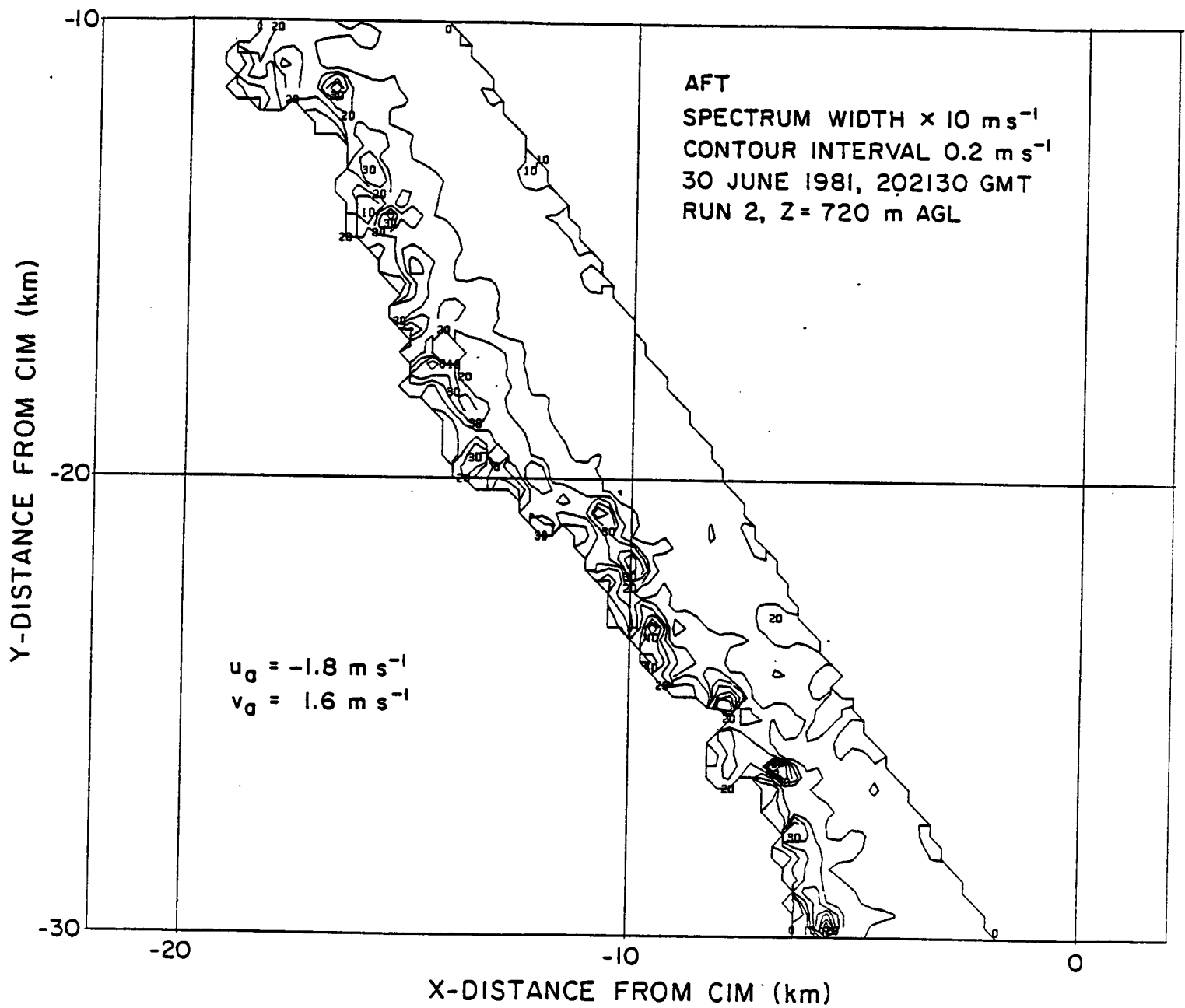
After application of (6) to the fore and aft spectral width data, the revised fore and aft fields of spectral width showed considerably more consistency of pattern and magnitude. Sample plots from run 2 are given in Figs. 3 and 4. In assessing the degree of agreement between fore and aft fields, we considered the fields to be in satisfactory agreement if they differed from each other by less than a factor of 2.5. This factor was a reasonable choice in view of the large fluctuations which characterized the spectral width in regions of high noise content.

FIG. 3. Modified spectral width from fore data, run 2, 30 June 1981.



ORIGINAL PAGE IS  
OF POOR QUALITY

FIG. 4. Modified spectral width from aft data, run 2, 30 June 1981.



## Chapter III

### OTHER ANALYSES

Several additional analyses were conducted in an effort to see if the lidar data yielded results which were self-consistent or conformed with either previous observations or theoretical calculations. Among these analyses were Lagrangian computations of parcel vorticity along the gust front of run 2, most unstable wavelength computations of vortex spacing along that same gust front, and examination of the divergence of wind components normal to arbitrarily oriented lines passing through the center of the asymmetric isolated cumulus cloud of runs 5-12.

#### 3.1. Vorticity analysis along the run 2 gust front

Particularly noteworthy features seen in some of the 1981 lidar results (Bluestein et al., 1985; McCaul, 1985; McCaul et al., 1987) are the well-defined vertical perturbations seen along the gust front of run 2 in the 30 June data. Peak vorticity in these features, computed from the gridded lidar winds, is about  $4 \times 10^{-2} \text{ s}^{-1}$ . Almost all the vortex patterns appear to be associated with notches or clefts in the arcus seen both in the side-looking photographs and in the reflectivity patterns, and thus appear to be genuine.

To further substantiate the observed vortex patterns and large vorticity concentrations along the gust front, we performed computations of parcel vorticity along parcel trajectories which seemed reasonable for such a gust front, and compared the results with the observations. To do this, we needed to estimate the vertical shear near the gust front, the vertical velocity at and near the front, the amount of convergence along the front, and the width of the convergence zone. Most of these quantities could be estimated from the lidar data or from data collected by a National Severe Storms Laboratory (NSSL) mesonet station at Tuttle-South (TTS), which was overflown by the aircraft during data collection.

Since the aircraft apparently was closest to TTS (within 1 km) at 2020 GMT, the average vertical shear at TTS was estimated by comparing the wind vectors obtained by the lidar and the surface station. The lidar-derived winds nearest TTS were  $4.3 \text{ m s}^{-1}$  from 135 deg at 2020 GMT, while the surface station's 60-s average wind was  $1.9 \text{ m s}^{-1}$  from 134 deg at that time. Using the aircraft altitude estimate of 722 m from the CV-990's down-looking radar and ignoring the tiny difference in wind azimuths, we infer a southeasterly vertical shear of  $3.3 \times 10^{-3} \text{ s}^{-1}$ .

We estimated the peak surface convergence and the width of the frontal convergence zone from consideration of the

front-normal velocity components of the winds shown in Fig. 5, under the assumption that the winds at TTS were representative of the overall two-dimensional average circulation across the front. Centered-difference computations on the 498 m one-dimensional grid that results from the time-to-space transformation (twice as coarse as the grid used to resolve the lidar measurements), yield convergence of  $7 \times 10^{-3} \text{ s}^{-1}$ , while the spatial pattern of the convergence estimates implies that the width of the convergence zone is about 2.1 km. This width is in agreement with the width of the zone of well-defined convergence measured by Hobbs and Persson (1982) along a cold front, but is about half that which was measured at the edge of a gust front studied by Fulton and Zrnic' (1985).

A peak convergence of about  $5 \times 10^{-2} \text{ s}^{-1}$  was inferred from the lidar winds near one of the gust front vortices, but typical lidar-derived values of convergence near the front were  $1-2 \times 10^{-2} \text{ s}^{-1}$ . These latter values are in good agreement with the magnitude of the TTS-derived surface convergence, especially when the differences in spatial resolution are taken into account. A firm estimate of the width of the convergence zone could not be obtained from the lidar-derived wind fields in run 2 because noise in the lidar winds masked the convergence patterns at about the  $10^{-3} \text{ s}^{-1}$  magnitude level.

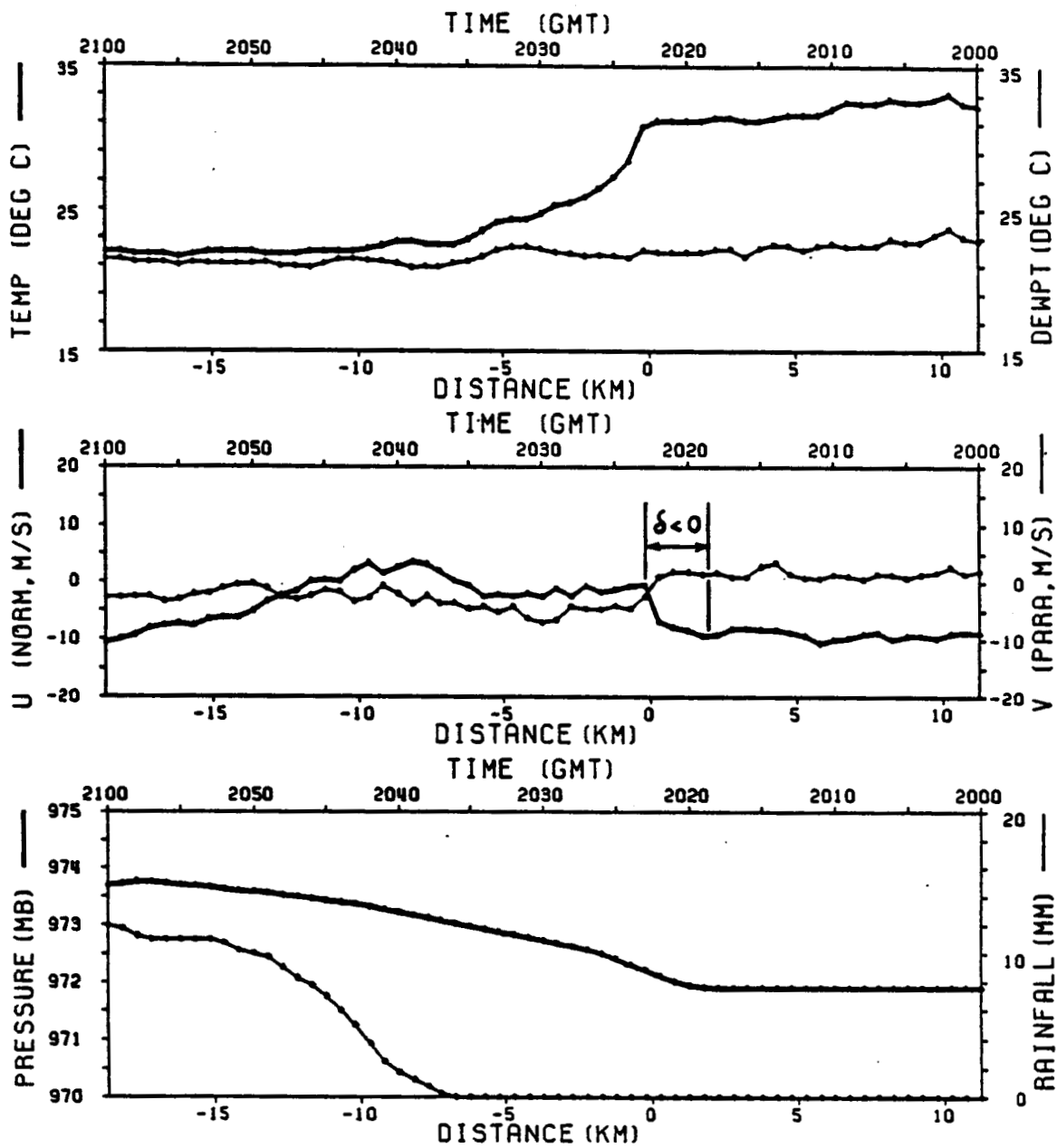


FIG. 5. Plot of meteorological observations from TTS (Tuttle South), 2000-2100 GMT, 30 June 1981. Pressure and rainfall traces have been smoothed with a three-point low-pass filter to reduce quantization effects. Traces of front-normal and front-parallel components of windspeed are also displayed (center panel), and the portion of the wind data corresponding to surface convergence is marked " $\delta < 0$ ."

We hypothesized that the gust front vortex patterns might be caused by the tilting of pre-existing horizontal vorticity in the boundary layer just ahead of the gust front, some of which may have been solenoidally generated (Rotunno and Klemp, 1985), or by hydrodynamic instability of the sheared interface between the warm and cold air on either side of the gust front. To see whether the magnitudes of vorticity computed from the lidar-derived run 2 winds can be explained by the tilting and stretching mechanisms, we consider these terms in the vorticity equation in height coordinates:

$$d\zeta/dt = -(\zeta + f)\delta - \hat{k} \cdot \nabla w \times \vec{\nabla}_h / dz \quad (7)$$

where:  $\zeta$  = vertical relative vorticity

$f$  = Coriolis parameter

$\delta$  = horizontal divergence

$\vec{\nabla}_h$  = horizontal wind vector

$w$  = vertical wind component

$\hat{k}$  = unit vector along z-coordinate

This equation is directly integrable for parcels traversing the gust front zone under the assumption of constant convergence and tilting of vertical shear. The solution is of the form:

$$\zeta = b (\exp(-\delta t) - 1) \quad (8)$$

where the coefficient  $b$  is given by  $f + (1/\delta)(\partial w/\partial x)(\partial v/\partial z)$ , with  $v$  the velocity component parallel to the gust front. Our assumptions constitute a simple conceptual model of the gust front vertical circulation derived from Goff (1975), in which both cold and warm air experience ascent along the frontal interface, with maximum upward motion occurring in the warm air within 1 km of the interface. Here, for simplicity, we assumed also that the interface was purely vertical throughout the lowest 720 m, and that maximum upward motion occurred at the interface, as observed by Fulton and Zrnic' (1985). We assumed that vorticity of parcels entering the gust front zone was initially equal only to the Coriolis parameter, and we used typical lidar- and TTS-derived values for  $\delta$  of  $10^{-2} \text{ s}^{-1}$  and  $|\partial \bar{V}_w / \partial z|$  of  $3 \times 10^{-3} \text{ s}^{-1}$  in the warm air near the gust front. Although vorticity could in principle be produced by tilting on both the warm and cold sides of the gust front, and subsequently advected toward the gust front boundary from both sides, we lacked estimates of vertical shear in the cold air and thus restrict our discussion to the effects of tilting of shear in the warm air only.

We assumed convergence was constant from the surface up to the aircraft altitude, 720 m, so that  $w = -z\delta$  from integration of the incompressible form of the mass continuity equation. It then followed that upward motions of about  $7 \text{ m s}^{-1}$  probably occurred along the gust front at

aircraft altitude. These upward velocities are within the range of values measured by Goff (1975) and Browning (1971) along gust fronts and cold fronts respectively.

Taking  $w$  at 360 m as an estimate of the mean vertical velocity experienced by parcels traversing the gust front zone, and using an updraft zone half-width of about 1.5 km, we estimated a mean  $|\nabla w|$  of  $2.4 \times 10^{-3} \text{ s}^{-1}$ , and a background vorticity production rate from tilting of  $7.2 \times 10^{-6} \text{ s}^{-2}$ . The solution (8) then showed that the exponentially growing vorticity reaches the observed value of  $10^{-2} \text{ s}^{-1}$  in only 260 s. This time is comparable to the 200 s required for a parcel to accelerate to a vertical velocity of 7 m  $\text{s}^{-1}$  while rising from near the surface up to aircraft altitude and simultaneously translating 1.5 km at a gust-front-relative speed of about 8 m  $\text{s}^{-1}$ . Thus it appears that tilting and stretching effects estimated using the lidar and TTS data are consistent in magnitude with the average gust front vorticity computed from the lidar winds.

We also investigated the vorticity budget of parcels traversing the gust front using a more detailed analytical model of the flow which obviated the need for the assumption of constant convergence during the traversal. We proceeded by considering the Lagrangian form of the vorticity equation:

$$\frac{d\zeta}{dt} = -(\zeta + f)\delta(x) - (\partial w(z,x)/\partial x)(\partial v/\partial z) \quad (9)$$

where we are now letting the convergence vary with across-front distance  $x$ , but not in the vertical, and we are letting the vertical velocity vary with both  $x$  and  $z$ . We now assume that the convergence pattern across the gust front may be modelled locally as a sine wave:

$$\delta(x) = \delta_0 \cos(\pi x / 2L) \quad (10)$$

where  $L$  is the distance from the front where convergence switches to divergence, and  $\delta_0$  is the value of divergence at the front, where it is largest (negative). Now since we are modelling the front as a line of convergence, we may express the divergence in terms of only one velocity component  $\delta(x) = \partial u / \partial x$ , from which we deduce:

$$u(x) = (2L\delta_0 / \pi) \sin(\pi x / 2L) \quad (11)$$

Because  $\dot{q} = \partial w / \partial z$ , we may thus find  $w$ :

$$w(x, z) = -\delta_0 z \cos(\pi x / 2L) \quad (12)$$

Therefore the  $\partial w / \partial x$  term in (9) becomes:

$$\partial w / \partial x = (\pi \delta_0 z / 2L) \sin(\pi x / 2L) \quad (13)$$

We next assume the flow is steady and is characterized by vorticity  $\zeta = \partial v / \partial x$  which is a function  $\zeta = \zeta(x, z_0)$ , where  $z_0$  is the altitude assumed by a parcel when it enters the gust front convergence zone located at  $x = L$ . Substitution of (10) and (13) into (9) under these assumptions leads to:

$$\begin{aligned} u \frac{\partial \zeta}{\partial x} + \delta \zeta &= (2\delta_0 L/\pi) (\partial \zeta / \partial x) \sin(\pi x / 2L) + \delta_0 \zeta \cos(\pi x / 2L) \\ &= -f \delta_0 \cos(\pi x / 2L) - (\pi \delta_0 z_0 / 2L) \partial v / \partial z \end{aligned} \quad (14)$$

Simplification of (14) results in:

$$d/dx \{ f \sin(\pi x / 2L) \} = -(\pi f / 2L) \cos(\pi x / 2L) - (\pi / 2L)^2 z_0 s_0 \quad (15)$$

where now  $s_0$  is the assumed constant value of  $\partial v / \partial z$ . Integrating (15) from  $x = L$  inward to some other  $x$  yields an expression for vorticity:

$$\begin{aligned} \zeta(x, z_0) &= f(1 - \sin(\pi x / 2L)) / \sin(\pi x / 2L) \\ &\quad + (\pi^2 / 4) (s_0 z_0 / L) (1 - x/L) / \sin(\pi x / 2L) \end{aligned} \quad (16)$$

If we now choose reasonable values of the parameters  $f$ ,  $s_0$  and  $L$  to be  $1 \times 10^{-4} \text{ s}^{-1}$ ,  $3 \times 10^{-3} \text{ s}^{-1}$  and 2 km respectively, we may compute the vorticity field on a cross section transverse to the gust front for various reasonable values of  $x/L$  and  $z/L$ . The results, given in Table 1, are in very close agreement with the mean value and distribution of vorticity across the gust front, as deduced from the lidar winds. In particular, at an altitude of 500 m ( $z/L = 0.25$ ) and a distance of 100 m from the front ( $x/L = 0.05$ ), the computed vorticity is about  $2.4 \times 10^{-2} \text{ s}^{-1}$ , very similar to the average value at the front seen in the lidar-derived vorticity results (McGaul, 1985). We conclude that the lidar data seem to be self-consistent and in agreement with what simple theoretical models would predict, at least as far as the gust front winds are concerned.

TABLE 1

x/L:	0.05	0.10	0.15	0.20	0.25
z/L					
0.25	0.0236	0.0112	0.0071	0.0050	0.0038
0.20	0.0191	0.0091	0.0057	0.0041	0.0031
0.15	0.0146	0.0069	0.0044	0.0031	0.0023
0.10	0.0101	0.0048	0.0030	0.0021	0.0016
0.05	0.0057	0.0027	0.0017	0.0012	0.0009

We now turn to the question of whether hydrodynamical instability of the Helmholtz type could have been responsible for the production of the gust front vortices. We recall that vortices qualitatively similar in appearance to those observed in run 2 have been observed by Carbone (1982, 1983) along an intense winter-time cold front in California, and by Wilson (1986) along a spring-time cold front in Colorado. In Carbone's data, peak vorticities and divergences were similar to those observed here, about  $10^{-2} \text{ s}^{-1}$ , but overall wind speeds were much higher and the flow was characterized by a strong jet parallel to the front. The vortices observed by Carbone were spaced at intervals of approximately 13 km, somewhat larger than the 3-10 km observed here. However, in the case studied by Wilson (1986), the spacing of vortices was in the middle of the range of spacings found here.

Carbone attributed the vortices to Helmholtz instability in the region of strong horizontal shear along the front. Barcilon and Drazin (1972) conclude, using standard linear stability analysis techniques, that shear zones which can be modelled as vertical vortex sheets are always unstable in the presence of superadiabatic lapse rates. Evidence from TTS temperature data and temperature data taken by the aircraft suggest that a slightly superadiabatic lapse rate of 10.6 deg C per km of altitude existed at TTS at 2020 GMT, just 2.5 min before the arrival of the gust front. Furthermore, if we model the gust front zone as a horizontal shear layer with a half-width, 0.75 km, constrained to agree with the TTS wind observations, linear theory predicts (Drazin and Reid, 1981, p. 146) a most unstable wavelength of 11 km, which is close to the maximum spacing seen in the run 2 winds (see Bluestein et al., 1985, or McCaul, 1985). Thus it appears possible that Helmholtz instability could have been responsible for the development of the vortical circulations observed in the run 2 lidar data. Vortices resembling Carbone's and those observed here have also been obtained along gust front shear zones in numerical simulations of convective clouds (R. Rotunno, National Center for Atmospheric Research (NCAR), 1985, personal communication).

### 3.2. Divergence near an isolated cumulus congestus

The 1981 lidar winds near an isolated cumulus congestus revealed that there was an overall pattern of cloud-scale convergence both below cloud base and at about mid-height of the cloud. The magnitude of cloud-scale convergence computed using only the mean wind vectors from each run at each level applied at the centroidal positions of the vector fields from each run was approximately  $4 \times 10^{-4} \text{ s}^{-1}$ . We sought further ways of seeing whether the lidar winds suffered from any unidirectional or sideways-pointing biases during the circumnavigations. One test we applied involved computing the divergence of wind components normal to axes which could be rotated to any orientation through the cloud center.

In order to compute the convergence normal to an arbitrarily oriented axis using the available lidar mean winds from each run, it was first necessary to establish the normal and parallel distances of the centroids of wind vector fields from the axis. Because the data runs were of differing lengths, these centroids were not symmetrically disposed about the axis in question. Thus it was not possible to obtain simple finite difference estimates of the axis-normal divergence, and a more general approach had to be developed. To compute the axis-normal divergence, we assumed that the axis-normal and axis-parallel wind

components were linear functions of along-axis distance. There were two data points available on either side of the arbitrary axis for use in computing the linearity coefficients and offsets. The normal velocity components on the "positive" side of the arbitrary axis were thus written:

$$v_p = a_{vp} \cdot x_{lp} + b_{vp} \quad (17)$$

while those on the "negative" side were written:

$$v_n = a_{vn} \cdot x_{ln} + b_{vn} \quad (18)$$

The coefficients  $a_{vp}$  and  $a_{vn}$  and offsets  $b_{vp}$  and  $b_{vn}$  are computed from:

$$a_{vp} = (v_{plp} - v_{p2p}) / (x_{l1p} - x_{l2p}) \quad (19)$$

$$b_{vp} = v_{plp} - a_{vp} \cdot x_{l1p} \quad (20)$$

$$a_{vn} = (v_{pln} - v_{p2n}) / (x_{l1n} - x_{l2n}) \quad (21)$$

$$b_{vn} = v_{pln} - a_{vn} \cdot x_{l1n} \quad (22)$$

where  $v_{plp}$  and  $v_{p2p}$  are the transverse velocity components at the two points on the "positive" side of the arbitrary axis and  $v_{pln}$  and  $v_{p2n}$  are the corresponding quantities on the "negative" side; the  $x_{l1p}$ ,  $x_{l2p}$ ,  $x_{l1n}$  and  $x_{l2n}$  are the corresponding longitudinal distances of each data run wind field centroid along the axis. Entirely analogous expressions for the distances  $x_p$  and  $x_n$  by which the centroids were off-axis, along with their linearity coefficients and offsets  $a_{xp}$ ,  $a_{xn}$ ,  $b_{xp}$  and  $b_{xn}$  were also written.

We then estimated the transverse-axis divergence along the longitudinal axis from:

$$\delta(x_1) = (v_p(x_1) - v_n(x_1)) / (x_p(x_1) - x_n(x_1)) \quad (23)$$

which reduces to the ratio of linear functions:

$$\delta(x_1) = \frac{(av_p - av_n)x_1 + (bv_p - bv_n)}{(ax_p - ax_n)x_1 + (bx_p - bx_n)} \quad (24)$$

The latter quantity could be integrated analytically to obtain an averaged value of the transverse divergence along the  $x_1$ -domain defined by the data points having coordinates farthest to the left and to the right of the origin (center of the circumnavigation). The final expression for the mean transverse divergence became:

$$\delta_n = (1/c^2) \{ (bc - ad) \ln((c \cdot x_{1max} + d) / (c \cdot x_{1min} - d)) + ac(x_{1max} - x_{1min}) \} / (x_{1max} - x_{1min}) \quad (25)$$

where  $a = av_p - av_n$ ,  $b = bv_p - bv_n$ ,  $c = ax_p - ax_n$ ,  $d = bx_p - bx_n$ , and  $x_{1max}$  and  $x_{1min}$  are the maximum and minimum data coordinates along the arbitrary axis. The computations of the mean transverse divergence given by (25) could then be made for a set of arbitrarily-oriented axes through the centroid of each circumnavigation in order to see whether the divergences showed any preferential axis of orientation.

Below cloud base, the mean convergence computed from the variation of the wind component normal to a line was

greatest for a line oriented north-northeast to south-southwest (Fig. 6, solid line). This line corresponds closely to the actual orientation of the cloud band. At mid-height of the cloud, however, the convergence is not concentrated along any direction (Fig. 6, dashed line).

The fact that the subcloud convergence showed a tendency to orient itself along an axis parallel to the observed cloud is further evidence that the lidar wind fields are indeed behaving like the true wind field. However, further independent verification of the lidar winds from cloud circumnavigations is desirable before all the details seen in the 1981 circumnavigations are accepted as correct.

DIVERGENCE ( $10^{xx-3}$ /SEC)

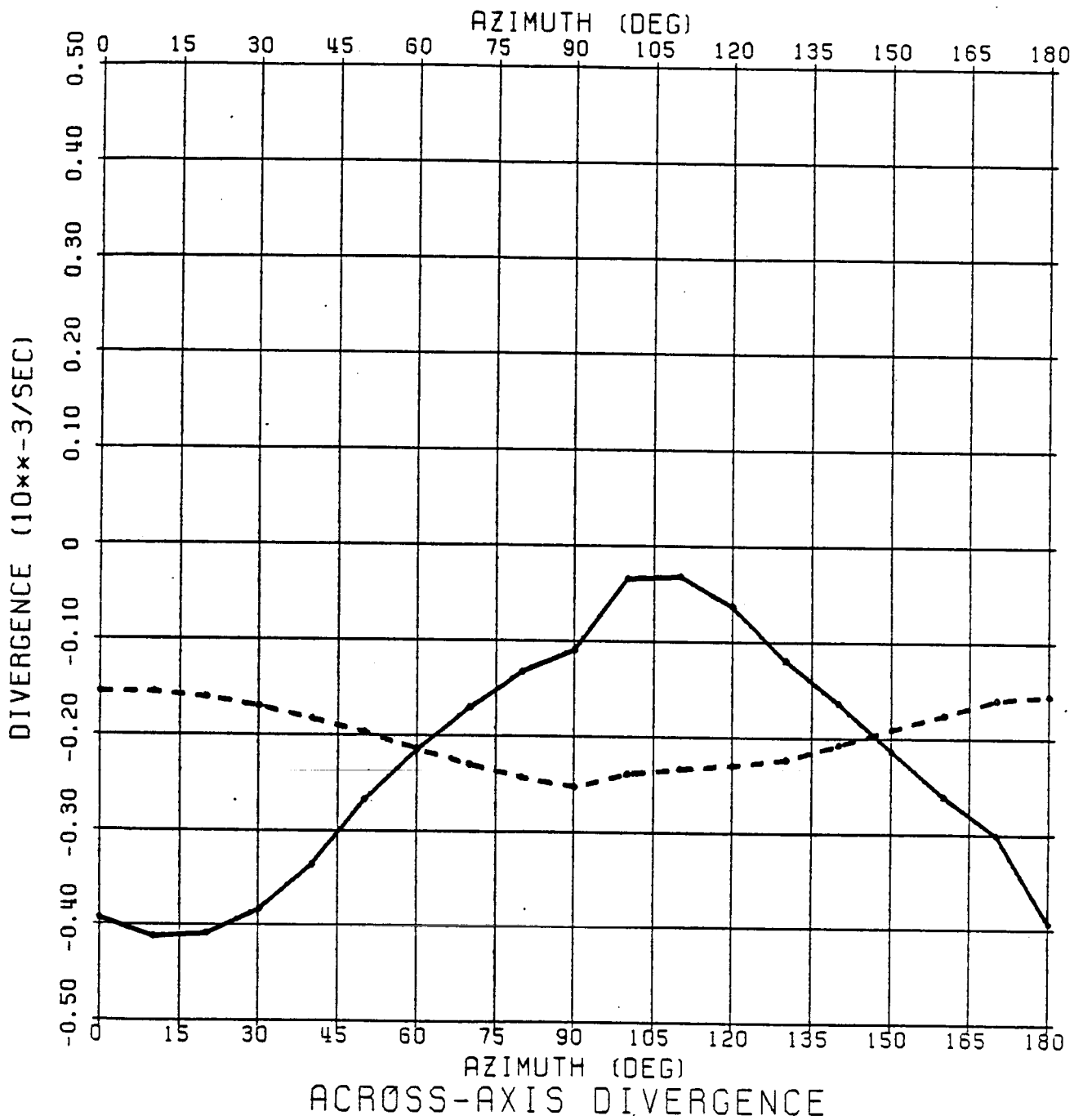


FIG. 6. Estimates of convergence due to variation of the wind component normal to lines of assumed orientation (azimuth). Solid line represents convergence inferred from sub-cloud winds near cumulus congestus, while dashed line represents corresponding results from around mid-height of the cloud.

## Chapter IV

### SUMMARY

Continued study of the lidar data collected in 1981 has resulted in significant new improvements in the analysis techniques reported by Bluestein et al. (1985) and McCaul (1985). Some of these improvements are reported in McCaul et al. (1986) and McCaul et al. (1987), but full details of the procedures and findings are not available in those references.

Through comparison of fore- and aft-derived scalar fields of intensity and spectral width, the self-consistency of the lidar moment estimates was assessed. Reflectivity estimates were found to be quite stable and reliable, while spectral widths were prone to become noisy if SNR fell below 12 dB. In addition, spectral widths contained a significant component due to radial velocity gradients in areas along gust fronts, and these components were different along the fore and aft lines of sight. Significant improvement in agreement between the fore and aft fields of spectral width was obtained by estimating the radial velocity gradient component and then removing it from the raw measured widths to yield only the turbulent portion of the contribution to width.

Additional analyses showed that lidar-derived vorticity estimates were consistent with several approximate models of vorticity growth along gust front zones, and with the hypothesis that Helmholtz instability could have been responsible for vortices seen along part of the gust front of 30 June 1981. Computations of divergence transverse to axes through an isolated cumulus congestus indicated that the strongest convergence tended to lie along an axis parallel to the congestus. This and the results of the other additional analyses seem to suggest that the lidar winds do indeed accurately reflect the basic features of the real wind field. Further work is recommended in order to determine the extent to which the lidar-derived wind field details are accurate.

## REFERENCES

- Barcilon, A. I. and P. G. Drazin, 1972: Dust devil formation. *Geophys. Fluid Dyn.*, 4, 147-158.
- Bluestein, H. B., R. J. Doviak, M. D. Eilts, E. W. McCaul, R. Rabin, A. Sundara-Rajan, and D. S. Zrnic', 1985: Analysis of airborne Doppler lidar, Doppler radar, and tall tower measurements of atmospheric flows in quiescent and stormy weather. *CIMMS Report and Contrib.* No. 62, Final Report to NASA, Research Contract No. NAS8-34749, 165 pp., (Available from CIMMS, 401 E. Boyd St., Norman, OK 73019). (also published as NASA Contractor Report 3960, Feb. 1986)
- Browning, K. A., 1971: Radar measurements of air motion near fronts. Part Two: Some categories of frontal air motion. *Weather*, 26, 320-340.
- Carbone, R. E., 1982: A severe frontal rainband. Part I: stormwide hydrodynamic structure. *J. Atmos. Sci.*, 39, 258-279.
- Carbone, R. E., 1983: A severe frontal rainband. Part II: tornado parent vortex circulation. *J. Atmos. Sci.*, 40, 2639-2654.
- Drazin, P. G., and W. H. Reid, 1981: *Hydrodynamic Stability*. Cambridge University Press, Cambridge, 525 pp.
- Fulton, R. A., and D. S. Zrnic', 1985: Structure of a thunderstorm surface outflow from single Doppler radar observations. *Preprints*, 14th Conf. Severe Local Storms, Indianapolis, IN, Amer. Meteor. Soc., 73-76.
- Goff, R. C., 1975: Thunderstorm outflow kinematics and dynamics. *NOAA Tech. Memo. ERL NSSL-75*, Norman, OK, 63 pp., (Available from NSSL, 1313 Halley Circle, Norman, OK 73069).
- Hobbs, P. V., and P. O. G. Persson, 1982: The mesoscale and microscale structure and organization of clouds and precipitation in midlatitude cyclones. Part V: The substructure of narrow cold-frontal rainbands. *J. Atmos. Sci.*, 39, 280-295.

- McCaull, E. W., Jr., 1985: Observations of Oklahoma convection using airborne Doppler lidar and ground-based Doppler radar. M. S. thesis, School of Meteorology, University of Oklahoma, Norman, OK 73019, 320 pp.
- McCaull, E. W., Jr., H. B. Bluestein and R. J. Doviak, 1986: Airborne Doppler lidar techniques for observing severe thunderstorms. *Appl. Optics*, 25, 698-708.
- McCaull, E. W., Jr., H. B. Bluestein and R. J. Doviak, 1987: Airborne Doppler lidar observations of convective phenomena in Oklahoma. *J. Atmos. Oceanic Technol.*, accepted for publication.
- Rotunno, R. and J. B. Klemp, 1985: On the rotation and propagation of simulated supercell thunderstorms. *J. Atmos. Sci.*, 42, 271-292.
- Wilson, J. W., 1986: Tornadogenesis by nonprecipitation induced wind shear lines. *Mon. Wea. Rev.*, 114, 270-284.

**Appendix A**  
**ABSTRACTS OF PAPERS RESULTING FROM THIS PROJECT**